Geophysical Research Letters

RESEARCH LETTER
10.1029/2022GL102209

**Key Points:**

- Signatures indicating reconnection onset can be identified in the electron distributions
- Onset signatures persist over extended spatial and temporal scales
- The particle distributions immediately preceding onset are characterized by features of non-gyrotropy and acceleration

**Supporting Information:**

Supporting Information may be found in the online version of this article.

**Correspondence to:**

S. F. Spinnangr,
susanne.spinnangr@uib.no

**Citation:**

Spinnangr, S. F., Hesse, M., Tenfjord, P., Norgren, C., Kolstø, H. M., Kwagala, N. K., et al. (2022). Electron behavior around the onset of magnetic reconnection. *Geophysical Research Letters*, *49*, e2022GL102209. https://doi.org/10.1029/2022GL102209

Received 21 NOV 2022
Accepted 1 DEC 2022



# Electron Behavior Around the Onset of Magnetic Reconnection

**Susanne F. Spinnangr[1], Michael Hesse[2], Paul Tenfjord[1], Cecilia Norgren[1], Håkon M. Kolstø[1], Norah K. Kwagala[1], Therese Moretto Jørgensen[2], and Tai Phan[3]**

[1]University of Bergen, Bergen, Norway, [2]NASA Ames Research Center, Mountain View, CA, USA, [3]Space Sciences Laboratory, UC Berkeley, Berkeley, CA, USA

**Abstract** We investigate the onset of magnetic reconnection, utilizing a fully kinetic Particle-In-Cell (PIC) simulation. Characteristic features of the electron phase-space distributions immediately before reconnection onset are identified. These include signatures of pressure non-gyrotropy in the velocity distributions, and lemon shaped distributions in the in-plane velocity directions. Further, we explain how these features form through particle energization by the out-of-plane electric field. Identification of these features in the distributions can aid in analysis of data where clear signatures of ongoing reconnection are not yet present.

**Plain Language Summary** In any environment where magnetic fields and charged particles interact, magnetic reconnection will occur if the conditions are favorable. Magnetic reconnection can be described as magnetic explosions, since it releases stored magnetic energy and converts it into heat and movement of the plasma particles. In this paper, we use numerical simulations to take a closer look at how the reconnection process initiates, a fundamental question still not fully understood.

## 1. Introduction

While magnetic reconnection is one of the most important energy conversion processes in our near space environment, on the Sun and in highly magnetized astrophysical plasmas, the question of what controls its onset is still not completely understood. Magnetic reconnection has been extensively modeled and observed in a large variety of plasma environments, such as planetary magnetospheres, the solar corona, astrophysical plasmas and in laboratories and fusion reactors on Earth (Yamada et al., 2010). If we want to understand how, where, and why magnetic reconnection occurs, we must understand what physical conditions are necessary for the onset of reconnection. It has been shown that magnetic reconnection needs thin current sheets to occur (e.g., Lui, 2004; Nakamura et al., 2006; Sitnov et al., 2019), but in-situ observations prove that this alone is not a sufficient criteria for reconnection onset (e.g., Paschmann et al., 2018; Phan et al., 2020; R. Wang et al., 2018).

The onset is difficult to study with spacecraft due to its explosive nature, and varied temporal and spatial scales. The majority of reconnection studies are performed at locations and times where the data already shows clear signatures of ongoing reconnection. These signatures include ion (e.g., Paschmann et al., 1979) and electron jets (Phan et al., 2007; Torbert et al., 2018), Hall magnetic and electric fields (Eastwood et al., 2010; Mozer et al., 2002; M. Øieroset et al., 2001; Wygant et al., 2005), and non-isotropic and non-gyrotropic particle distributions (e.g., Burch, Torbert, et al., 2016; Chen et al., 2016; Hesse et al., 2021; Li et al., 2019; Shuster et al., 2015; Z. Wang et al., 2019).

Some simulation studies have aimed to understand the physics of reconnection onset. Hesse et al. (2001) show that the presence of non-gyrotropy in the electron pressure is necessary for the generation of the diffusive electric field in the location where the X-line will form. This electron non-gyrotropy generates a linear instability of the system which eventually causes the onset of reconnection. A thorough study of the effect of the ion to electron mass ratio and the strength of the driving, was presented in Liu et al. (2014). They found that the slow change in $B_z$ prior to onset, and the rapid evolution after onset were unaffected by the mass ratio. They did however find that the time of the reconnection onset was strongly influenced by the mass ratio. This difference in onset time allowed them to identify the instability leading to reconnection onset as electron tearing. The importance of electron dynamics in reconnection onset was even further emphasized by Lu et al. (2020), who show both through observation and simulation that full scale magnetic reconnection initiates from electron-only reconnection in the presence of a strong external driver.

In this study, we investigate the electron dynamics right before the initial formation of an X-line, to identify signatures that are indicative of an imminent onset of reconnection. Recognizing such signatures will aid in the classification of reconnecting and non-reconnecting current sheets, which can broaden our understanding of what conditions are necessary for reconnection onset. In the following section we describe our simulation setup. In Section 3, we identify when onset occurs, then we discuss onset signatures in the electron phase space distributions in Section 4, while Section 5 is a summary and discussion about our results.

## 2. Simulation Design

We simulate magnetic reconnection in the magnetotail using a fully kinetic, 2.5D Particle-In-Cell (PIC) simulation. In our coordinate system, $x$ is the reconnection outflow direction, $y$ is the initial current direction, and $z$ is the inflow direction. Our simulation starts with a tail-like equilibrium (Birn et al., 1975) with oppositely directed magnetic fields and a current sheet with no perturbation. The initial magnetic field configuration is given by

$$B_x = \alpha(x)\tanh\left(\alpha(x)\frac{z}{l}\right) \tag{1}$$

$$B_z = \alpha'(x)\left(-z\tanh\left(\alpha(x)\frac{z}{l}\right) + \frac{l}{\alpha(x)}\right) \tag{2}$$

$$\alpha(x) = \left(1 + \frac{bx}{\gamma l}\right)^{-\gamma} \tag{3}$$

where $l = 2\ d_i$ is the half-width of the current sheet, $b = 0.05$, and $\gamma = 0.6$. To establish converging flow toward the current sheet, the top, bottom and left boundaries of the simulation domain are subjected to an electric field driver, given by

$$Left: \quad E_l(x = 0, z, t) = \Gamma(t)\left(\frac{z}{z_{\max}}\right)^2 b_{xl} \tag{4}$$

$$Top: \quad E_t\,(x, z = z_{\max}, t) = \Gamma(t)|\frac{x_{\max} - x}{x_{\max}}|b_{xt} \tag{5}$$

$$Bottom: \quad E_b\,(x, z = -z_{\max}, t) = \Gamma(t)|\frac{x_{\max} - x}{x_{\max}}|b_{xb} \tag{6}$$

which increases the asymptotic magnetic field strength ($B_x$) through Faraday's law and leads to current sheet thinning. The $b_x$ terms are expressions for the z-average of $B_x$ in the boundary cells, $\Gamma(t) = \tanh(0.1t)/\cosh^2(0.1t)$, and $t$ is time. The electric field driver peaks around $t = 7$ before it falls off, such that the driving phase is over around $t = 35$, long before the system eventually reconnects. Similar driving mechanisms that mimic the loading of magnetic flux in the inflow regions by the solar wind have been employed in previous studies, successfully resulting in reconnection (e.g., Hesse et al., 2001; Liu et al., 2014; Pritchett, 2005, 2010). The particular form of the driving can influence the timing of the onset and the location of the x-point, but the kinetic physics of the onset should remain unaffected when the driver is turned off early.

Lengths are normalized to the ion inertial length, $d_i = \frac{c}{\omega_{pi}}$, where $\omega_{pi} = \sqrt{\frac{n_0 e^2}{\epsilon_0 m_i}}$ is the ion plasma frequency with $n_0$ being the initial current sheet density and $m_i$ is the ion mass. Time is normalized to the inverse ion cyclotron frequency, $\Omega_i^{-1} = \frac{m_i}{eB_0}$, where $B_0$ is the initial asymptotic magnetic field. We employ a time step of $\omega_{pe}\delta t = 1$. Densities are normalized to $n_0$, velocities to the ion Alfvén velocity, $v_A = B_0/\sqrt{\mu_0 m_i n_0}$, and kinetic energies to $m_i v_A^2$. The boundary conditions are reflective in both the inflow and outflow directions. We use a total of $6.7 \times 10^9$ macro-particles. The size of the simulation domain is $60\ d_i \times 20\ d_i$ divided into a grid of $2{,}048 \times 1{,}024$ cells, resulting in about 3,200 particles per cell. The ions and electrons have a mass ratio of $\frac{m_i}{m_e} = 100$ and their temperature ratio is $\frac{T_e}{T_i} = 0.2$. The ratio of the ion plasma frequency to the electron cyclotron frequency is $\omega_{pe}/\Omega_e = 2$.

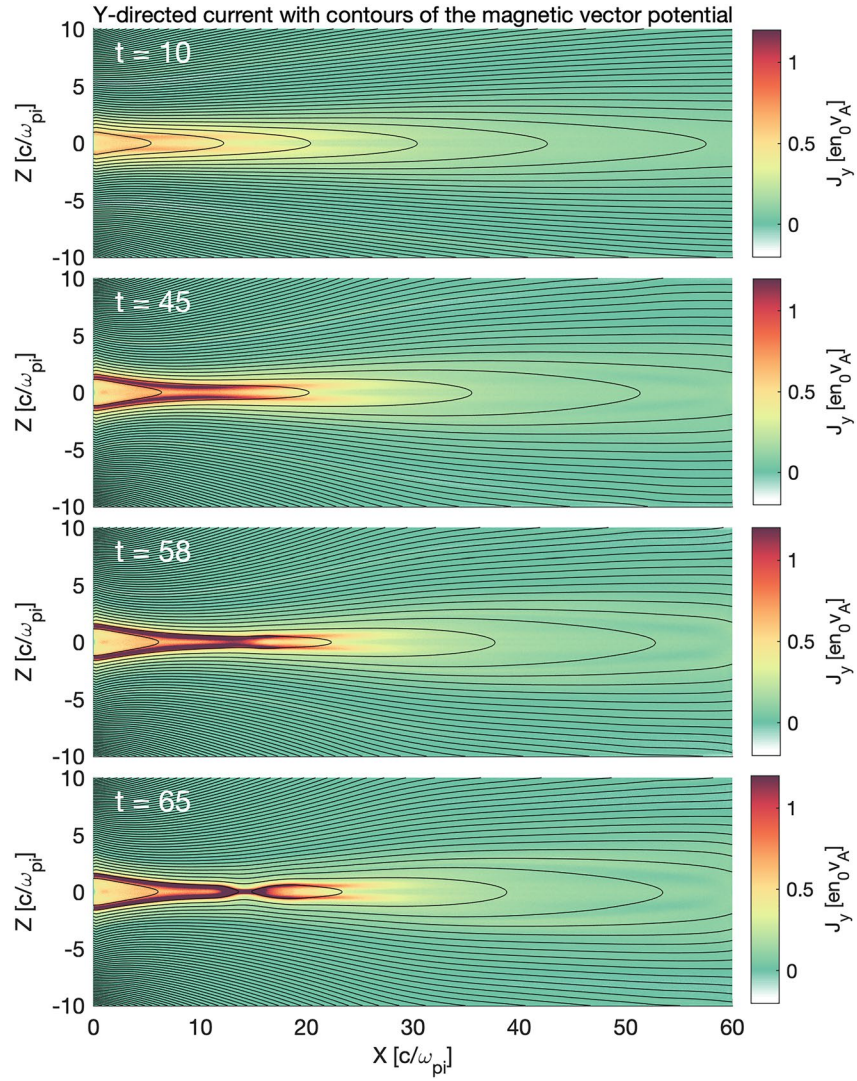


**Figure 1.** Evolution of the in-plane magnetic field (contours) and out-of-plane current density $J_y$ (color). The current sheet becomes thinner and eventually reconnects. The penultimate panel shows the time of investigation, $t = 58\ \Omega_i^{-1}$, discussed later in the paper.

In Figure 1 we show an overview of the in-plane magnetic field (contour lines) and out-of-plane current $J_y$ (color), for four different times. We see how the thick current sheet becomes thinner as the magnetic field in the asymptotic regions become stronger, and that the thinning continues after the driving phase is over, until reconnection occurs. The penultimate panel in Figure 1 shows the simulation at the time ($t = 58$) we will investigate in detail in the following analysis.

## 3. Onset of Reconnection

To investigate the onset of magnetic reconnection, we must first determine when onset occurs. We follow a similar tactic as employed in (Liu et al., 2014). In our set up, the direction of $B_z$ is initially <0 everywhere. In order for $B_z > 0$ to appear at the neutral plane ($z = 0$), reconnection must have occurred. We therefore determine the time of investigation by finding the maximum value of $B_z(x, z = 0)$ (Figure 2a), as a function of time. An X-line forms as the max value of $B_z$ intersects 0, which is marked in the figure with a horizontal dotted line, after which reconnection is definitely ongoing. Liu et al. (2014) determined the onset time by comparing the behavior of $B_z$ to a stable reference simulation in which reconnection did not occur. Onset was defined as the time when the behavior of $B_z$ started to deviate significantly from this reference run, in which $B_z$ just showed a smooth change

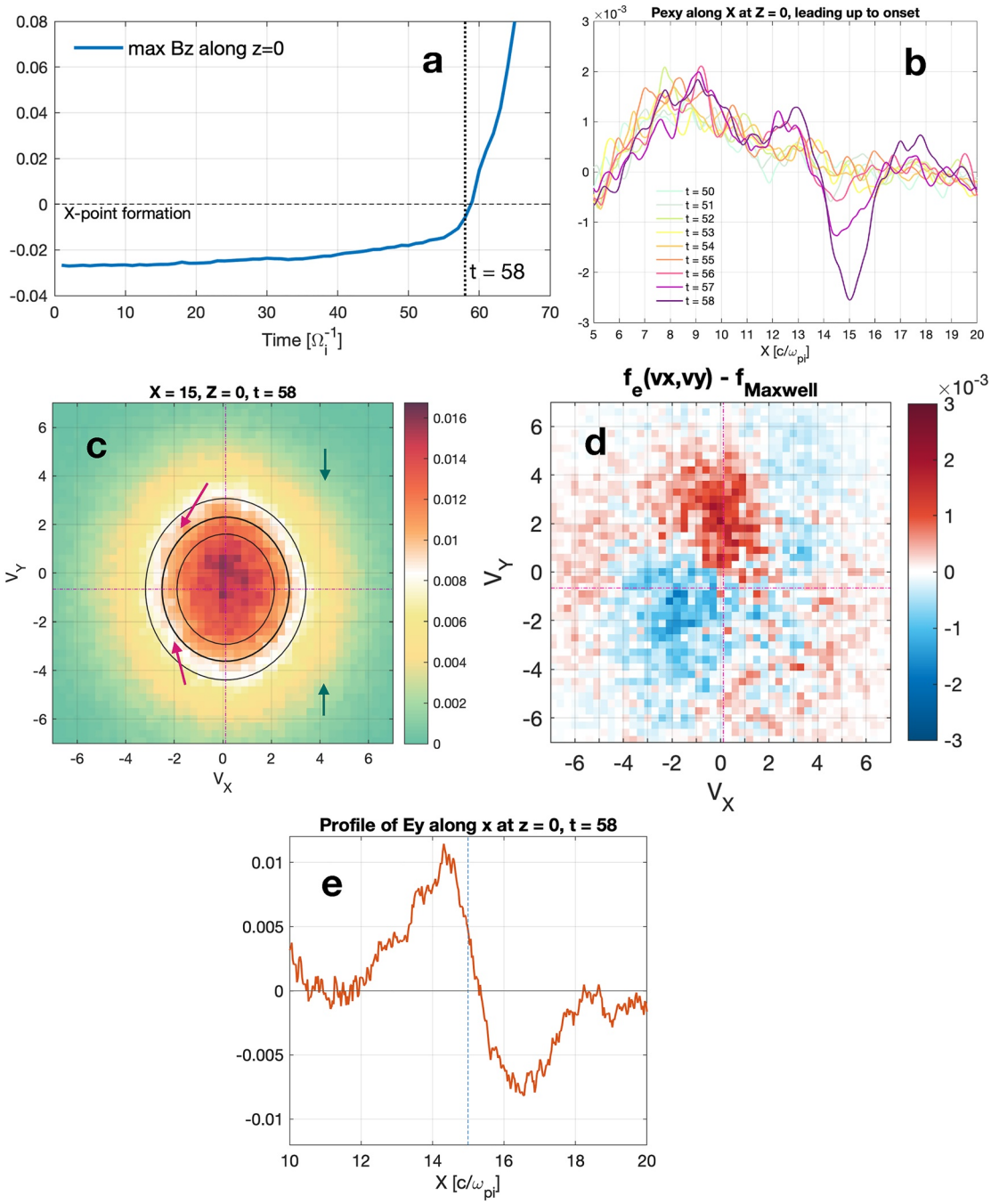


**Figure 2.** (a) Maximum value of $B_z$ along $z = 0$ as a function of time. When we see a significant change in the slope of this value we are close to reconnection onset. We define the time of investigation as the last output time before the formation of the X-line (indicated by the dotted line). (b) Cut through $z = 0$ of $P_{exy}$, for different times leading up to the onset. The data has been averaged with a running mean in order to remove noise and extract the average behavior. We see the necessary gradient for the generation of a diffusive electric field starts to appear and grow bigger from $t = 56$. (c) $f_e(v_x, v_y)$ at $x = 15$, $z = 0$ and $t = 58$. The dotted pink lines show the bulk velocity. The three black contour lines show how the distribution would look if it was purely bi-Maxwellian. (d) The difference between the distribution in (c) and the corresponding bi-Maxwellian distribution. (e) The reconnection electric field along $x$ at $z = 0$ and $t = 58$. The data is averaged over 0.5 $d_i$ in the $z$-direction to reduce noise. We see that the amplitude of $E_y$ is higher to the left of where the X-line forms than to the right. This is also true for earlier times (not shown).

with a fairly even slope. This is similar to what we see in Figure 2a until $t \approx 55$. We have chosen to treat the last output time of our simulation before the X-line forms as the time of investigation, to ensure that we will see the system in the immediate pre-reconnection state. The time of investigation is $t = 58$, which is marked in Figure 2a with a vertical dotted line.

Next we study the off-diagonal electron pressure tensor. Magnetic reconnection can only happen in a small diffusion region where an electric field parallel to the current direction dominates the particle dynamics. This electric field is often referred to as the reconnection electric field or the diffusive electric field, and is necessary to break the frozen in condition and allow particles to diffuse across magnetic field lines. This reconnection electric field is generated through the non-gyrotropic contributions of the electron pressure tensor (Hesse et al., 1999, 2001; Kuznetsova et al., 1998; Vasyliunas, 1975). In our setup, this electric field can be expressed as

$$E_y = -\frac{1}{n_e e}\left(\frac{\partial P_{exy}}{\partial x} + \frac{\partial P_{eyz}}{\partial z}\right). \tag{7}$$

The dominating contribution around reconnection onset comes from $\partial P_{exy}/\partial x$ (Hesse et al., 2001). Figure 2b shows $P_{exy}$ along the $x$-axis at $z = 0$ for the times leading up to the reconnection onset. A clear increase in $P_{exy}$ starts to form at $t = 56$, and a significant peak is present at $x = 15$ and $t = 58$, the chosen time of investigation. The existence of this peak and consequently the gradient along $x$ around it confirms that our choice of investigation time is appropriate. In the following analysis of the electron behavior, we will investigate phase space distributions centered around this peak in $P_{exy}$.

## 4. Particle Behavior

In the preceding section we saw that a reconnection X-line forms close to $x = 15$ and $z = 0$. To investigate the electron behavior leading up onset, we select boxes centered around this point in which we construct the distribution functions in phase space. The boxes have $dx = 0.125\ d_i$ and $dz = 0.05\ d_i$ in each direction from their center value, such that the total length and height of each box is $0.25\ d_i$ and $0.1\ d_i$ respectively. The box sizes were chosen to optimize the resolution of the distributions without loosing statistics by having too few particles in each box. Figures 3 and 4 show maps of the reduced distribution functions $f_e(v_x, v_y)$ and $f_e(v_x, v_z)$, respectively, at $t = 58$. For completeness, a corresponding map in the $v_y v_z$ plane is included as Figure S1. In the following, we will discuss features in these distributions.

As can be seen in Figure 3, $f_e(v_x, v_y)$ is fairly similar in the different locations. This means that the features we will point out are present not only at the exact location where the X-line forms, but in a larger area around it. To aid in the analysis of the smaller scale electron behavior, we choose to use the center distribution as an example.

Figure 2c shows $f_e(v_x, v_y)$ centered around $x = 15$ and $z = 0$, at $t = 58$. The most prominent feature we see is a shift toward the negative $v_y$-direction. The two dotted pink lines show the bulk flow. Previously, we found that $P_{exy} \neq 0$ at this location and time. We therefore expect the distribution to show non-gyrotropic features. However, since the relative magnitude of the non-gyrotropic pressure to the total pressure is small ($P_{exy}/P_{exx} \approx 3\%$), these features are subtle. To make them easier to identify, we have overlaid the contours of a corresponding bi-Maxwellian distribution, centered at the bulk flow. As it is the higher energy parts of the distribution that provide the largest contribution to the pressure, we are more interested in the features we see further away from the center than the peak around the bulk flow. For particles with negative $v_x$, we see a clear asymmetry between the top and bottom quadrants, indicated by the two magenta arrows. A similar, but opposite asymmetry is found for particles with positive $v_x$ where the green arrows are pointing. If we imagine the distribution is divided vertically along the x-directed bulk flow into two semicircles, we see that the result of the asymmetries is that the two halves are shifted along the $v_y$-direction with respect to each other. A similar feature was found by Hesse et al. (2011) for guide field reconnection. An additional way of illustrating this is provided in Figure 2d, showing the difference between the distribution and the corresponding bi-Maxwellian from 2c.

We can explain the shifted semicircles by investigating the history of the particles making up the distribution. In Figure 2e we show a cut of $E_y(x, z = 0, t = 58)$. The data has been averaged over $\pm 0.5\ d_i$ in the inflow direction to reduce noise. The dotted blue line shows the x-location of the box in which we took the discussed distribution. As we can see, $E_y$ is positive in this location, as well as to the left of it, while it turns negative to the right at $x > 15.3$. In the region $z = 0$, $x > 18$, $E_y = -(\mathbf{v}_e \times \mathbf{B})_y$ (not shown), as the formation of a local minimum in $B_z$ causes the frozen-in electrons to convect tailwards here. However, the reversal we see between $x = 12$ and $x = 18$ is also supported by the pressure divergence and the temporal inertia. The electrons are accelerated anti-parallel to $E_y$. This means that the electrons entering the box centered at $x = 15$ from the right with negative $v_x$ are accelerated in the positive $y$-direction, while electrons entering from the left with positive $v_x$ are accelerated in the

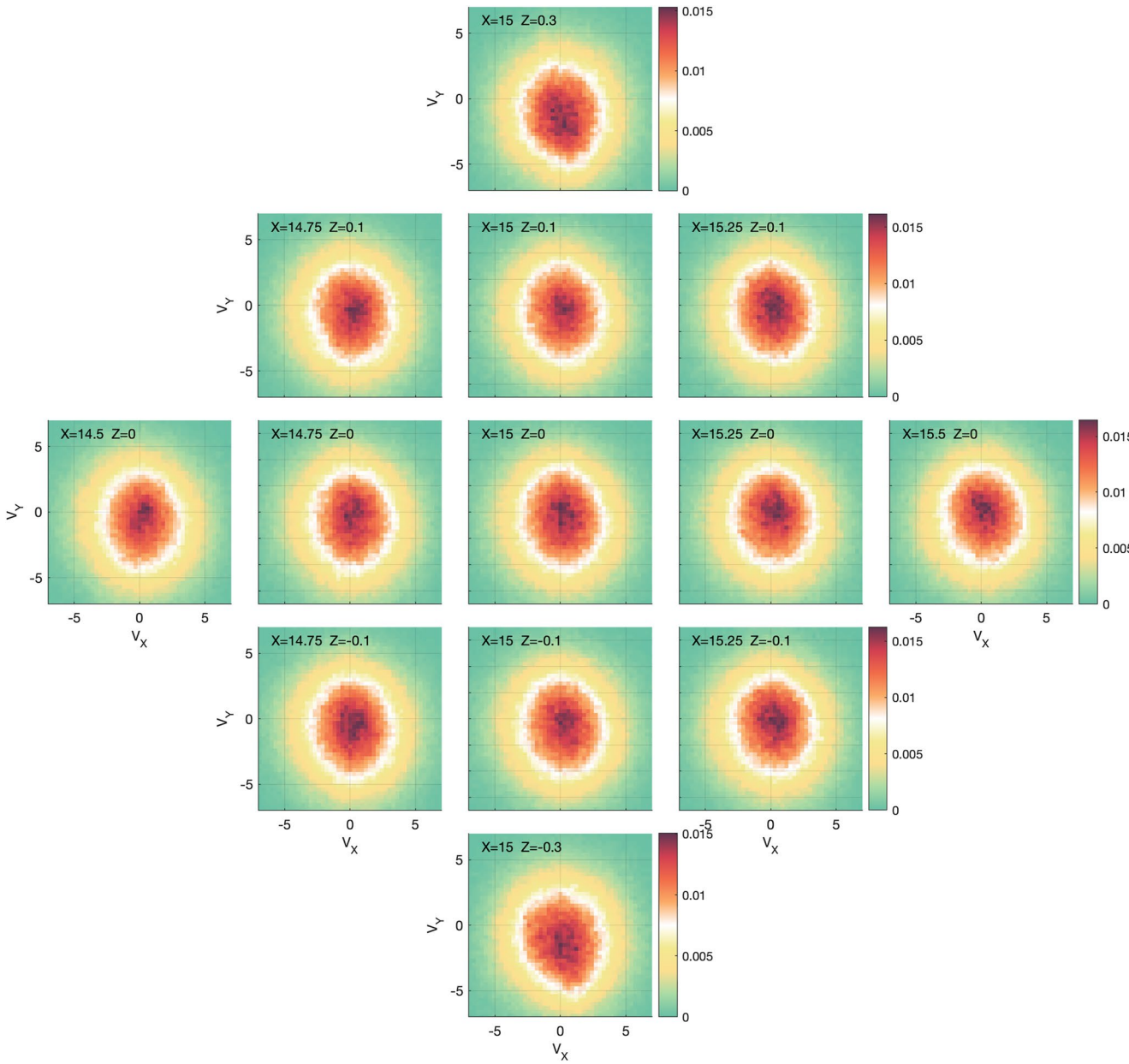


**Figure 3.** Reduced distributions $f_e(v_x, v_y)$ centered around the point where the contribution to the reconnection electric field from the non-gyrotropic pressure reaches a maximum at $t = 58$. The location of the center of each box is given in the top left corner of each distribution.

negative $y$-direction. Additionally, the magnitude of $E_y$ is on average slightly higher to the left of the box location than to the right. This means that particles entering this location from the left with positive $v_x$ have on average experienced more acceleration by $E_y$ than the particles coming from the right with negative $v_x$. This explains the non-gyrotropic feature of $f_e(v_x, v_y)$.

This feature is visible along the $z = 0$ plane, but as can be seen in Figure 3, it is even clearer as we move out in the inflow direction. This is likely because the magnitude of $E_y$ is greater at the boundaries where we see a larger gradient in $B_x$, which we will discuss below.

Figure 4 shows a map of $f_e(v_x, v_z)$ for the same locations as in Figure 3. As with $f_e(v_x, v_y)$, we see that the distributions display fairly similar features in all the locations. The most prominent feature is an elongation along the $v_z$-axis around $v_x = 0$, resulting in lemon-shaped distributions. This tells us that particles with none or very small

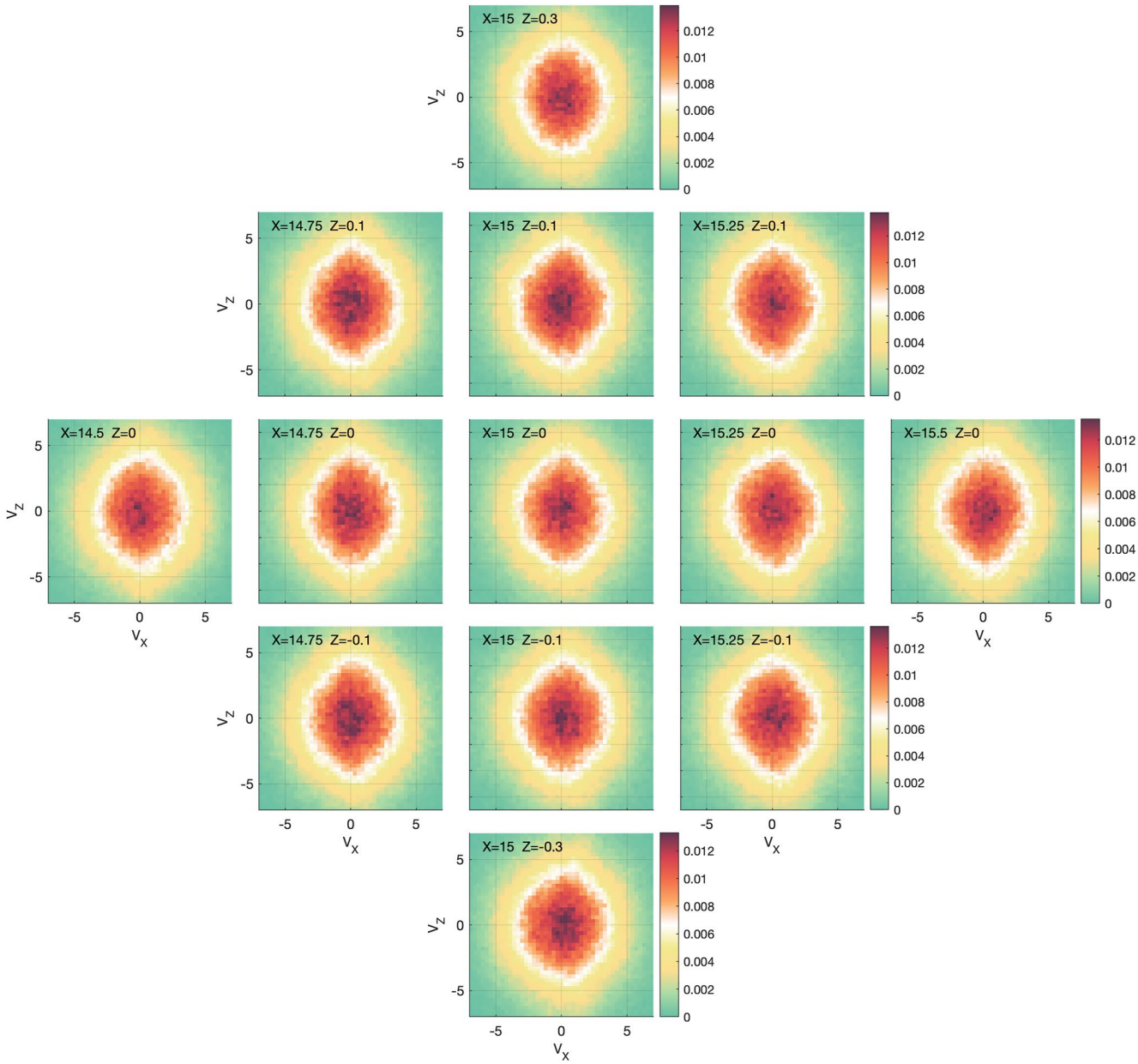


**Figure 4.** A map of $f_e(v_x, v_z)$ for the same boxes as in Figure 3 at $t = 58$.

$v_x$ are experiencing larger acceleration in the $z$-direction. To explain this lemon shape, we investigate how the particles are being energized.

In Figure 5 we again choose the distribution at $x = 15$, $z = 0$ as an example to discuss the features we see in all the distributions in Figure 4. In Figure 5a, we have chosen a test-particle to trace backwards in time to investigate how it gained the accelerated $v_z$, indicated by the star. Figure 5c through 5g show the particle position, kinetic energy, and the work done on the particle by the electric field, $-\int \mathbf{E}\cdot\mathbf{v}dt$, from a time long before the onset up to the investigation time. We see that the particle has a general drift in the negative $y$-direction, while it is bouncing in the $z$-direction and mirroring in the $x$-direction. The amplitude of the bouncing in $z$ is fairly constant through the full time interval, although we do see a general change toward smaller amplitudes from about $t = 54$ and onward. Figure 5b shows cuts along $z$, through $x = 15$, of $E_y$ averaged over 0.5 $d_i$ in $x$, plotted as a function of time. The black contour lines are the contours of the magnetic vector potential, indicating the motion of the magnetic field at this $x$. The two green dotted lines indicate where $z = 0.5\ d_i$ for comparison with the particle position. We see

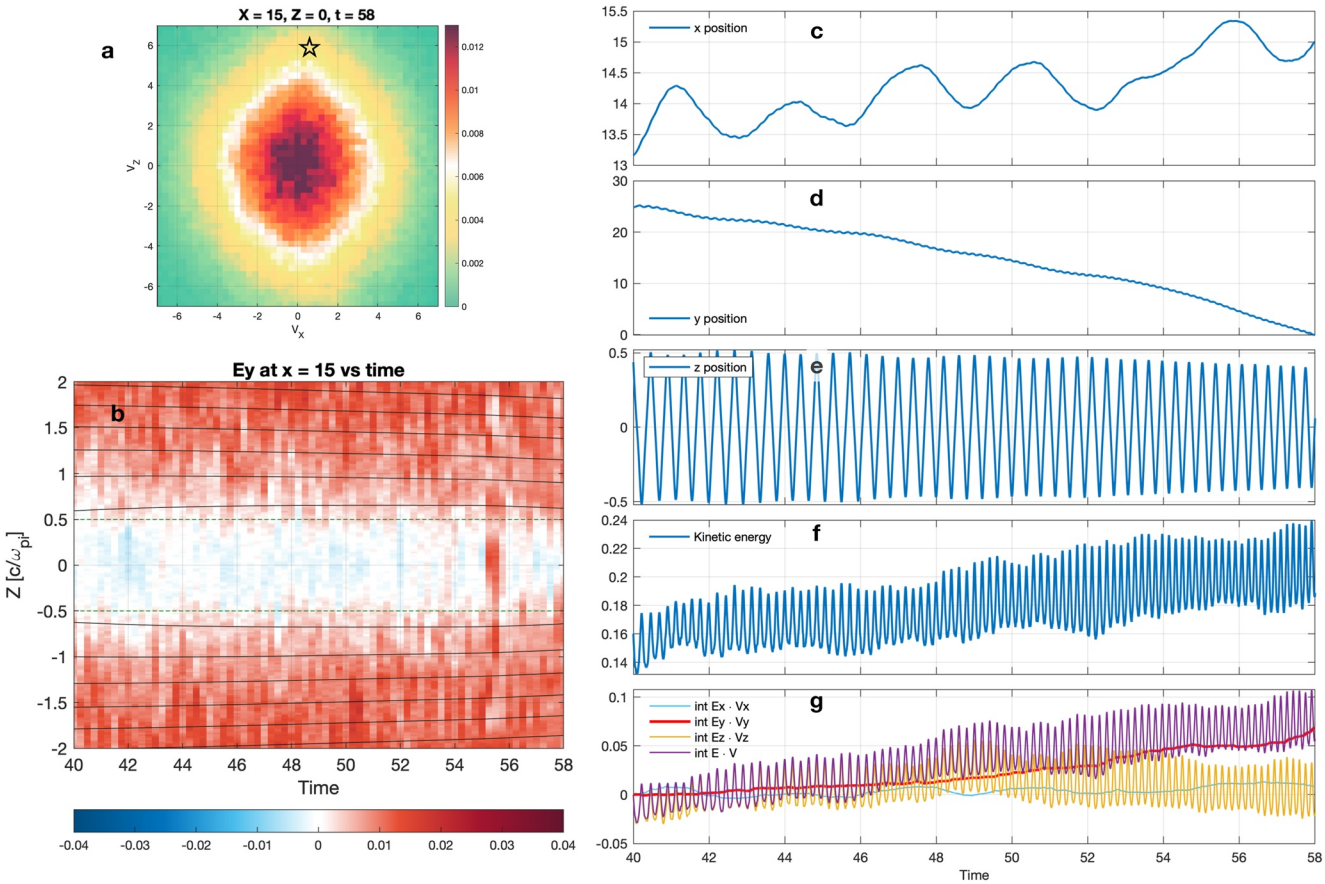


**Figure 5.** (a) $f_e(v_x, v_z)$ at $x = 15$, $z = 0$, $t = 58$. (b) Slices along $z$ at $x = 15$ of $E_y$ (averaged over 0.5 $d_i$ in $x$), plotted as a function of time, with contours of the magnetic potential. (c–g) Position, kinetic energy and $\int \mathbf{E} \cdot \mathbf{v} dt$ for a test-particle, as a function of time.

that $E_y$ is mostly negative and close to 0 in the center, while it is positive and with a larger amplitude further out. This is consistent with the evolution of the thinning current layer. The boundary between the positive and negative $E_y$ regions is fairly stationary until around $t = 56$, when it starts to move inwards. The short burst of positive $E_y$ in the center just before this is a transient, temporary, large-scale fluctuation that dissipates before the time of investigation, possibly caused by reflecting waves resulting from the driving.

Comparing the position of the turning point in the $z$-direction with the shape of the $E_y$ profile, we see that it coincides with the region where $E_y$ turns positive. A closer look at the work terms in Figure 5g reveals that the increase in kinetic energy comes from interactions with $E_y$, which results from the changing $B_x$. As the current sheet thins, $B_x$ above and below it increases and propagates toward the center. This leads to a build up of $E_y$ through Faraday's law. At the turning points in $z$, the particle motion is parallel to $E_y$, leading to energy gain through $\mathbf{E} \cdot \mathbf{v}$, as can be seen in Figure 5g. As the particle continues its meandering motion, this energy gain by $E_y$ is turned into an increased $v_z$ through the Lorentz force, $ev_yB_x$. The acceleration by $E_y$ thus manifests as the lemon shaped distribution in the $f_e(v_x, v_z)$. In Figure 5b, we also see the contours of the magnetic field start to move inwards and become closer together, with an increasing rate after about $t = 54$. Comparing this to the movement of the particle in $z$, we see the same behavior in the amplitude of the meandering motion. This shows that the particle bounces between the magnetic walls of the inflow magnetic field. As the meandering in $z$ and the propagation of the magnetic walls are oppositely aligned, this energy gain through $E_y$ can also be described as simple Fermi acceleration (Fermi, 1949; Northrop, 1963). Fermi acceleration between moving regions of increased magnetic field is a common acceleration mechanism in space plasmas in general, and has recently been used to describe acceleration of electrons inside magnetic islands (Drake et al., 2006) and between merging flux ropes (Arnold et al., 2021).

## 5. Summary and Discussion

This study is part of a larger effort to understand why, when and where magnetic reconnection occurs. To answer these questions we must understand why some current sheets reconnect while others do not. The results of this study may help to expand our pool of data to investigate in this regard. By being able to identify current sheets that are close to or at reconnection onset, data from current sheet observations that were previously discarded since they do not show signatures of ongoing reconnection could be included in analyses of reconnecting current sheets.

We identified two key signatures of reconnection onset in the electron distribution functions in our simulation. The first is non-gyrotropy in $f_e(v_x, v_y)$, seen as shifted semicircles along the $y$-directed bulk flow, consistent with the necessary gradient in the non-gyrotropic electron pressure contribution to the reconnecting electric field. The second signature is lemon shaped distributions in $f_e(v_x, v_z)$ due to Fermi acceleration of the electrons bouncing between the inward propagating magnetic field of the inflow regions. Later in our simulation (not shown), the electron distributions transition to exhibit the typical signatures of active reconnection, such as distinct counter-streaming electrons in the direction normal to the current sheet, cigar shapes in the inflow region and emerging crescents (e.g., Egedal et al., 2013; Shuster et al., 2015; Torbert et al., 2018). In principle, it is possible that lemon shapes in $f_e(v_x, v_z)$ could be generated in a non-reconnecting, thinning current sheet. Therefore, we note that both the non-gyrotropy and lemon shapes should be present simultaneously in a thinning current sheet for it to be an indicator of reconnection onset.

In our setup, the onset signatures are clear. We have confirmed that the results discussed in this paper are not affected by the boundary conditions. The temporal resolution of the Magnetospheric Multiscale satellites (MMS) is on electron scales (Burch, Moore, et al., 2016; Pollock et al., 2016), which is high enough that the signatures could be resolved. If we assume $B_0 = 20$ nT and $n_0 \sim 0.3$–$0.8$ cm$^{-3}$ (Toledo-Redondo et al., 2021), one ion cyclotron time in our simulation corresponds to about 3 $s$, and one ion inertial length corresponds to 255–420 km. The identified onset signatures in our simulation persist over several ion times and at least a full ion inertial length around the forming X-line, which increases the probability of detection. Identifying currents sheets that show signs of being close to reconnection onset would enable us to include them in research of reconnecting currents sheets, which might further our understanding of which conditions are necessary for reconnection to occur.

## Data Availability Statement

The data used in this study was created using Fortran90. Replication data and instructions on how to use it is available at the data repository site DataverseNO, via Spinnangr (2022).

**Acknowledgments**
This study was supported by NOTUR/NORSTOR under project NN9496K. SFS, CN, PT, and HK received support from the Research Council of Norway under contract 300865.

## References

Arnold, H., Drake, J. F., Swisdak, M., Guo, F., Dahlin, J. T., Chen, B., et al. (2021). Electron acceleration during macroscale magnetic reconnection. *Physical Review Letters*, *126*(13), 135101. https://doi.org/10.1103/PhysRevLett.126.135101

Birn, J., Sommer, R., & Schindler, K. (1975). Open and closed magnetospheric tail configurations and their stability. *Astrophysics and Space Science*, *35*(2), 389–402. https://doi.org/10.1007/bf00637005

Burch, J. L., Moore, T. E., Torbert, R. B., & Giles, B. L. (2016). Magnetospheric multiscale overview and science objectives. *Space Science Reviews*, *199*(No. 1–4), 5–21. https://doi.org/10.1007/s11214-015-0164-9

Burch, J. L., Torbert, R. B., Phan, T. D., Chen, L. J., Moore, T. E., Ergun, R. E., et al. (2016). Electron-scale measurements of magnetic reconnection in space. *Science*, *352*(6290). https://doi.org/10.1126/science.aaf2939

Chen, L. J., Hesse, M., Wang, S., Bessho, N., & Daughton, W. (2016). Electron energization and structure of the diffusion region during asymmetric reconnection. *Geophysical Research Letters*, *43*(6), 2405–2412. https://doi.org/10.1002/2016GL068243

Drake, J. F., Swisdak, M., Schoeffler, K. M., Rogers, B. N., & Kobayashi, S. (2006). Formation of secondary islands during magnetic reconnection. *Geophysical Research Letters*, *33*(13), 10–13. https://doi.org/10.1029/2006GL025957

Eastwood, J. P., Phan, T. D., Øieroset, M., & Shay, M. A. (2010). Average properties of the magnetic reconnection ion diffusion region in the Earth's magnetotail: The 2001-2005 Cluster observations and comparison with simulations. *Journal of Geophysical Research*, *115*(8), 1–13. https://doi.org/10.1029/2009JA014962

Egedal, J., Le, A., & Daughton, W. (2013). A review of pressure anisotropy caused by electron trapping in collisionless plasma, and its implications for magnetic reconnection. *Physics of Plasmas*, *20*(6), 1–18. https://doi.org/10.1063/1.4811092

Fermi, E. (1949). On the origin of the cosmic radiation. *Physical Review*, *75*(8), 1169–1174. https://doi.org/10.1063/1.3066619

Hesse, M., Kuznetsova, M., & Birn, J. (2001). Particle-in-cell simulations of three-dimensional collisionless magnetic reconnection. *Journal of Geophysical Research*, *106*(A12), 29831–29841. https://doi.org/10.1029/2001ja000075

Hesse, M., Neukirch, T., Schindler, K., Kuznetsova, M., & Zenitani, S. (2011). The diffusion region in collisionless magnetic reconnection. *Space Science Reviews*, *160*(1–4), 3–23. https://doi.org/10.1007/s11214-010-9740-1

Hesse, M., Norgren, C., Tenfjord, P., Burch, J. L., Liu, Y. H., Bessho, N., et al. (2021). A new look at the electron diffusion region in asymmetric magnetic reconnection. *Journal of Geophysical Research: Space Physics*, *126*(2), 1–16. https://doi.org/10.1029/2020JA028456

Hesse, M., Schindler, K., Birn, J., & Kuznetsova, M. (1999). The diffusion region in collisionless magnetic reconnection. *Physics of Plasmas*, *6*(5), 1781–1795. https://doi.org/10.1063/1.873436

Kuznetsova, M. M., Hesse, M., & Winske, D. (1998). Kinetic quasi-viscous and bulk flow inertia effects in collisionless magnetotail reconnection. *Journal of Geophysical Research*, *103*(A1), 199–213. https://doi.org/10.1029/97ja02699

Li, X., Wang, R., Lu, Q., Hwang, K. J., Zong, Q., Russell, C. T., & Wang, S. (2019). Observation of nongyrotropic electron distribution across the electron diffusion region in the magnetotail reconnection. *Geophysical Research Letters*, *46*(24), 14263–14273. https://doi.org/10.1029/2019GL085014

Liu, Y. H., Birn, J., Daughton, W., Hesse, M., & Schindler, K. (2014). Onset of reconnection in the near magnetotail: PIC simulations. *Journal of Geophysical Research: Space Physics*, *119*(12), 9773–9789. https://doi.org/10.1002/2014JA020492

Lu, S., Wang, R., Lu, Q., Angelopoulos, V., Nakamura, R., Artemyev, A. V., et al. (2020). Magnetotail reconnection onset caused by electron kinetics with a strong external driver. *Nature Communications*, *11*(1), 1–7. https://doi.org/10.1038/s41467-020-18787-w

Lui, A. T. Y. (2004). Potential plasma instabilities for substorm expansion onsets. *Space Science Reviews*, *113*(1/2), 127–206. https://doi.org/10.1023/b:spac.0000042942.00362.4e

Mozer, F. S., Bale, S. D., & Phan, T. D. (2002). Evidence of diffusion regions at a subsolar magnetopause crossing. *Physical Review Letters*, *89*(1), 1–4. https://doi.org/10.1103/PhysRevLett.89.015002

Nakamura, R., Baumjohann, W., Runov, A., & Asano, Y. (2006). Thin current sheets in the magnetotail observed by cluster. *Space Science Reviews*, *122*(1–4), 29–38. https://doi.org/10.1007/s11214-006-6219-1

Northrop, T. G. (1963). Adiabatic charged-particle motion. *Reviews of Geophysics*, *I*(August), 283. https://doi.org/10.1029/rg001i003p00283

Øieroset, M., Phan, T. D., Fujimoto, M., Lin, R. P., & Lepping, R. P. (2001). In situ detection of reconnection in the Earth's magnetotail. *Nature*, *412*(July), 414–417. https://doi.org/10.1038/35086520

Paschmann, G., Haaland, S. E., Phan, T. D., Sonnerup, B. U., Burch, J. L., Torbert, R. B., et al. (2018). Large-scale survey of the structure of the dayside magnetopause by MMS. *Journal of Geophysical Research: Space Physics*, *123*(3), 2018–2033. https://doi.org/10.1002/2017JA025121

Paschmann, G., Sonnerup, B. U., Papamastorakis, I., Sckopke, N., Haerendel, G., Bame, S. J., et al. (1979). Plasma acceleration at the Earth's magnetopause: Evidence for reconnection. *Nature*, *282*(5736), 243–246. https://doi.org/10.1038/282243a0

Phan, T. D., Bale, S. D., Eastwood, J. P., Lavraud, B., Drake, J. F., Oieroset, M., et al. (2020). Parker solar probe in situ observations of magnetic reconnection exhausts during encounter 1. *The Astrophysical Journal - Supplement Series*, *246*(2), 34. https://doi.org/10.3847/1538-4365/ab55ee

Phan, T. D., Drake, J. F., Shay, M. A., Mozer, F. S., & Eastwood, J. P. (2007). Evidence for an elongated (>60 ion skin depths) electron diffusion region during fast magnetic reconnection. *Physical Review Letters*, *99*(25), 1–4. https://doi.org/10.1103/PhysRevLett.99.255002

Pollock, C., Moore, T., Jacques, A., Burch, J., Gliese, U., Saito, Y., et al. (2016). Fast plasma investigation for magnetospheric multiscale. *Space Science Reviews*, *199*(1–4), 331–406. https://doi.org/10.1007/s11214-016-0245-4

Pritchett, P. L. (2005). Externally driven magnetic reconnection in the presence of a normal magnetic field. *Journal of Geophysical Research*, *110*(A5), A05209. https://doi.org/10.1029/2004JA010948

Pritchett, P. L. (2010). Onset of magnetic reconnection in the presence of a normal magnetic field: Realistic ion to electron mass ratio. *Journal of Geophysical Research*, *115*(10), 1–9. https://doi.org/10.1029/2010JA015371

Shuster, J. R., Chen, L. J., Hesse, M., Argall, M. R., Daughton, W., Torbert, R. B., & Bessho, N. (2015). Spatiotemporal evolution of electron characteristics in the electron diffusion region of magnetic reconnection: Implications for acceleration and heating. *Geophysical Research Letters*, *42*(8), 2586–2593. https://doi.org/10.1002/2015GL063601

Sitnov, M., Birn, J., Ferdousi, B., Gordeev, E., Khotyaintsev, Y., Merkin, V., et al. (2019). Explosive magnetotail activity. *Space Science Reviews*, *215*(4), 31. https://doi.org/10.1007/s11214-019-0599-5

Spinnangr, S. F. (2022). Replication data for: Electron behaviour around the onset of magnetic reconnection. *DataverseNO*. https://doi.org/10.18710/Z2XUSW

Toledo-Redondo, S., André, M., Aunai, N., Chappell, C. R., Dargent, J., Fuselier, S. A., et al. (2021). Impacts of ionospheric ions on magnetic reconnection and Earth's magnetosphere dynamics. *Reviews of Geophysics*, *59*(3). https://doi.org/10.1029/2020rg000707

Torbert, R. B., Burch, J. L., Phan, T. D., Hesse, M., Argall, M. R., Shuster, J., et al. (2018). Electron-scale dynamics of the diffusion region during symmetric magnetic reconnection in space. *Science*, *362*(6421), 1391–1395. https://doi.org/10.1126/science.aat2998

Vasyliunas, V. M. (1975). Theoretical models of magnetic field line merging. *Reviews of Geophysics*, *13*(1), 303–336. https://doi.org/10.1029/RG013i001p00303

Wang, R., Lu, Q., Nakamura, R., Baumjohann, W., Huang, C., Russell, C. T., et al. (2018). An electron-scale current sheet without bursty reconnection signatures observed in the near-earth tail. *Geophysical Research Letters*, *45*(10), 4542–4549. https://doi.org/10.1002/2017GL076330

Wang, Z., Fu, H. S., Liu, C. M., Liu, Y. Y., Cozzani, G., Giles, B. L., et al. (2019). Electron distribution functions around a reconnection X-line resolved by the FOTE method. *Geophysical Research Letters*, *46*(3), 1195–1204. https://doi.org/10.1029/2018GL081708

Wygant, J. R., Cattell, C. A., Lysak, R., Song, Y., Dombeck, J., McFadden, J., et al. (2005). Cluster observations of an intense normal component of the electric field at a thin reconnecting current sheet in the tail and its role in the shock-like acceleration of the ion fluid into the separatrix region. *Journal of Geophysical Research*, *110*(A9), 1–30. https://doi.org/10.1029/2004JA010708

Yamada, M., Kulsrud, R., & Ji, H. (2010). Magnetic reconnection. *Reviews of Modern Physics*, *82*(1), 603–664. https://doi.org/10.1103/RevModPhys.82.603